Supporting Information

Supporting Information includes SEM micrographs (Figure S1), XRD patterns of s-MnO_x precursor after calcination at different temperatures (Figure S2), pore size distributions of all samples (Figure S3), NEXAFS spectra of reference manganese oxides (Figure S4), s-MnO_x (Figure S5), s-MnO_x/$MWCNT_{ox}$ (Figure S6), i-MnO_x/$MWCNT_{ox}$ (Figure S7) during temperature treatment, Raman spectra of s-MnO_x/$MWCNT_{ox}$ and i-MnO_x/$MWCNT_{ox}$ (Figure S8), Mn 2p XP spectra of s-MnO_x, s-MnO_x/$MWCNT_{ox}$, i-MnO_x/$MWCNT_{ox}$ during temperature treatment (Figures S9-11) and C 1s XP spectra (Figure S12).

SEM

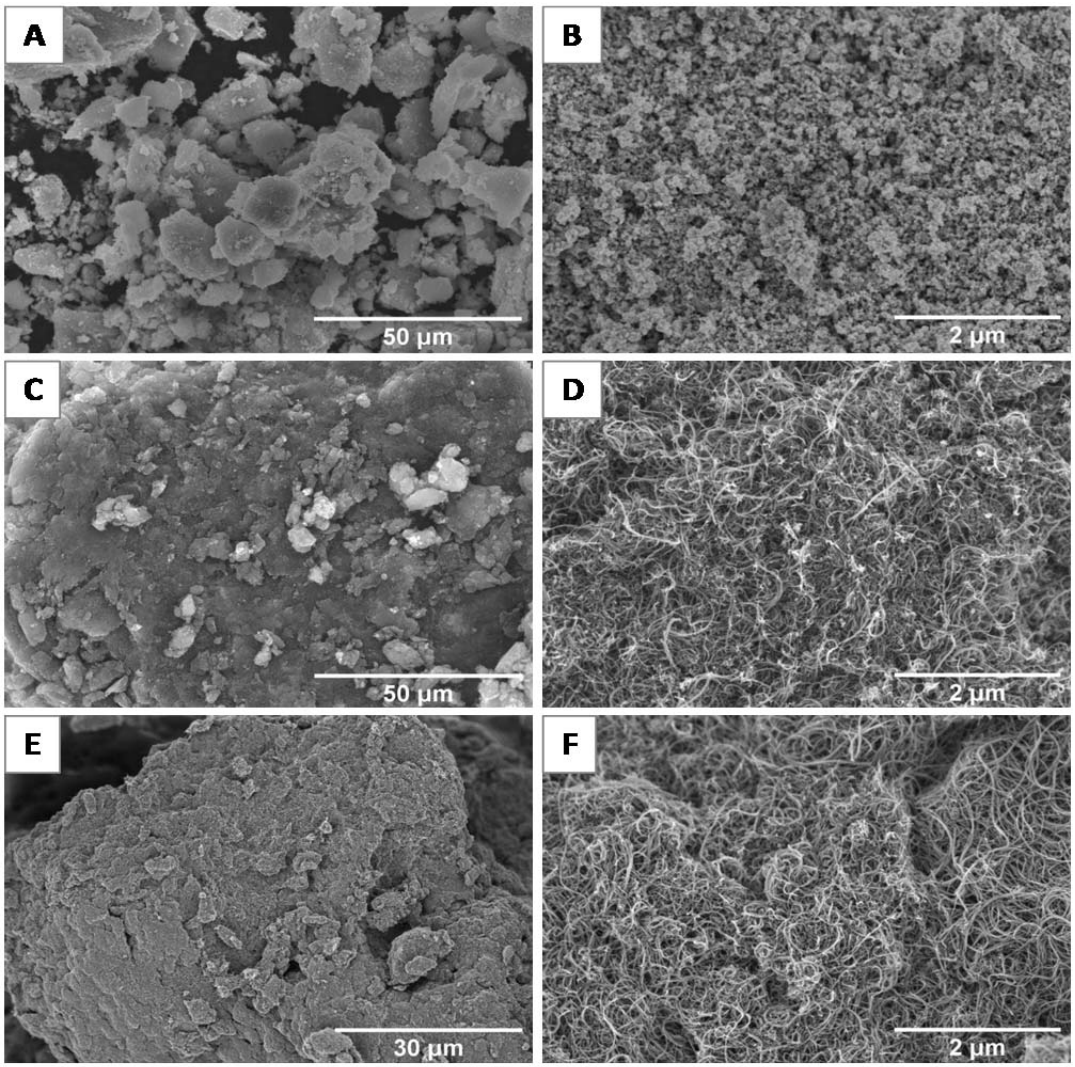

Figure S1. SEM micrographs of: s-MnO_x (A, B), s-MnO_x/$MWCNT_{ox}$ (C, D), i-MnO_x/$MWCNT_{ox}$ (E, F).

XRD

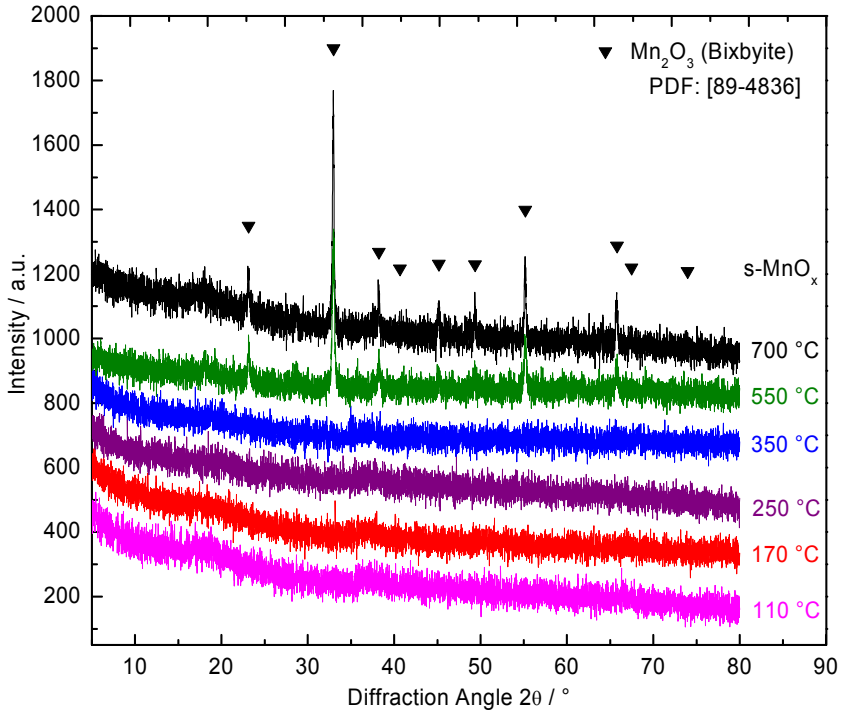

Figure S2. XRD patterns of the symproportionation precursor after calcination at different temperatures and after heating to 700 °C during TGA. The final product can be identified as Mn_2O_3 (Bixbyite, black triangles).

N_2-Physisorption – Pore Size Distribution

The BET surface area, determined by N_2 physisorption, decreased from 316 m^2/g for the pure MWCNTox to 240 m^2/g after deposition of Mn oxide. The s-MnOx/MWCNTox sample presents a typical type IV isotherm, with a clear hysteresis at high P/P_0. The pore size distribution calculated from the desorption branch of the isotherm using the BJH method shows a bimodal distribution (Figure S3). Pores below a diameter of 3 nm are assigned to the inner channel of the nanotubes, whereas larger pores > 10 nm are formed between the entangled nanotubes [1]. Figure S3 reveals that the volume of the small pores decreased after deposition of the Mn oxide. The most likely explanation is that MnOx particles also formed at the tubes tips as well as inside the CNTs, thus blocking the inner channel of some of the CNTs. As expected, the isotherm of the impregnated i-MnO_x/$MWCNT_{ox}$ shows a typical mesoporous carbon hysteresis of type IV [2]. The pore size distribution calculated from the desorption branch of the isotherm using the BJH method shows a bimodal distribution (Figure S3). On the one hand small pores between 1.5 and 4 nm diameter, which correspond to the inner channel of the nanotubes, on the other hand larger pores of 9 to 100 nm, which are formed between the entangled nanotubes [3].

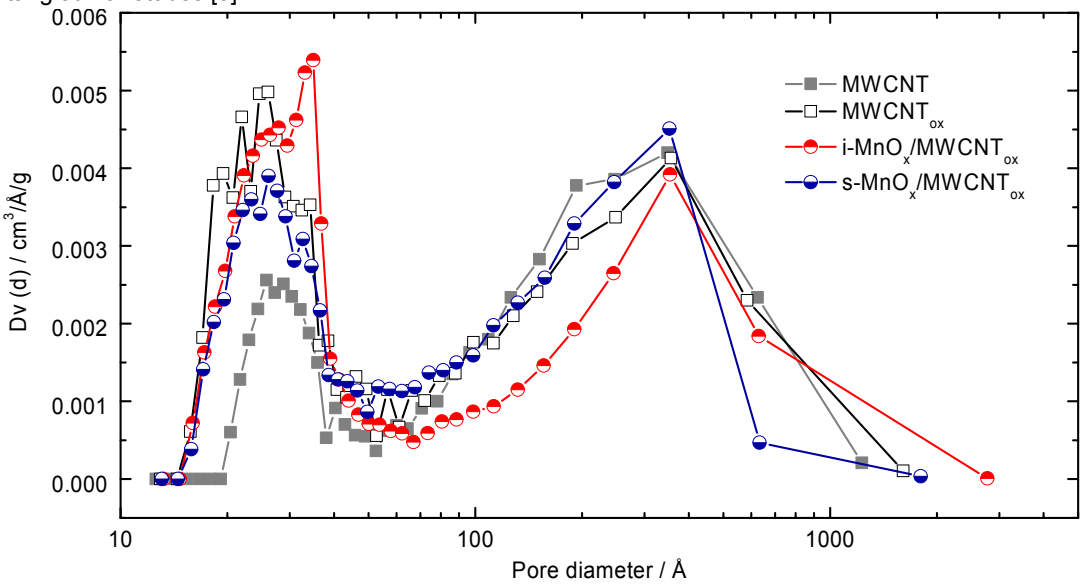

Figure S3. Pore size distributions of MWCNT, $MWCNT_{ox}$, s-MnO_x/$MWCNT_{ox}$ and i-MnO_x/$MWCNT_{ox}$ samples.

NEXAFS

The experimental spectra were fitted with a linear combination of spectra representing Mn^{2+}, Mn^{3+} and Mn^{4+} single valence sites. The resulting fit profiles have been extracted from the data set under the assumption, that pure Mn^{2+} is present in the sample impregnated with $Mn(NO_3)_2$, Mn^{3+} is formed upon oxidation of this sample and that no Mn^{2+} is present after heating the symproportionated sample to 400 °C in oxygen.
In Figure S4, the resulting fitprofiles are compared to those of reference Mn-oxide materials MnO and MnO_2 (commercial powders) and a reasonable agreement was found. The Mn^{3+} spectrum was extracted from the Mn^{2+} and Mn^{4+} oxides. Using these reference materials themselves for fitting the NEXAFS spectra, however, resulted in significantly poorer agreement, which can be explained by the contribution of the local geometry to the spectrum [4], which varies in different polymorphs of Mn-oxides and may not be representative for the prepared materials. This has also been observed in studies of other mixed valence systems [5].

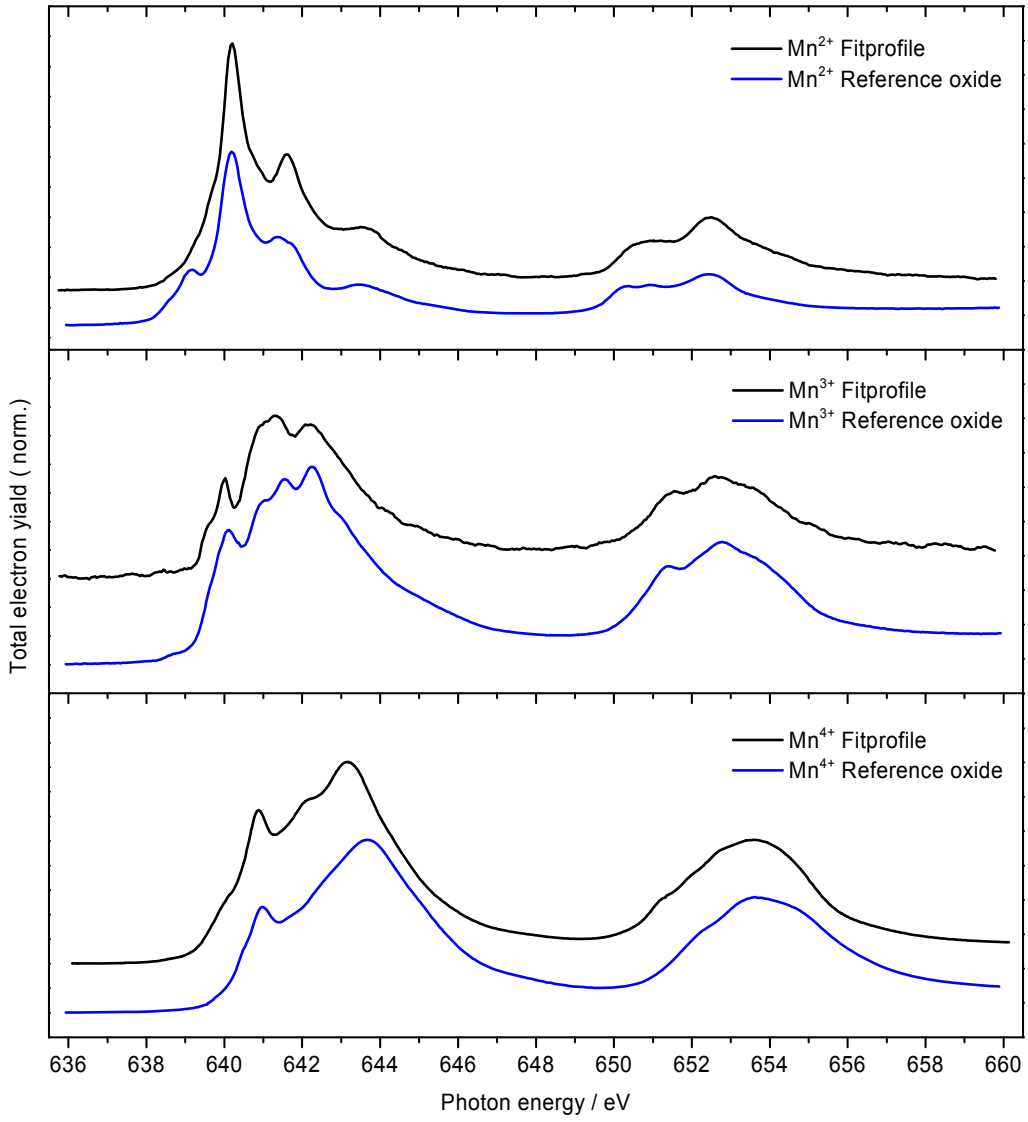

Figure S4. Mn L-NEXAFS spectra of fitted manganese oxides and reference manganese oxides.

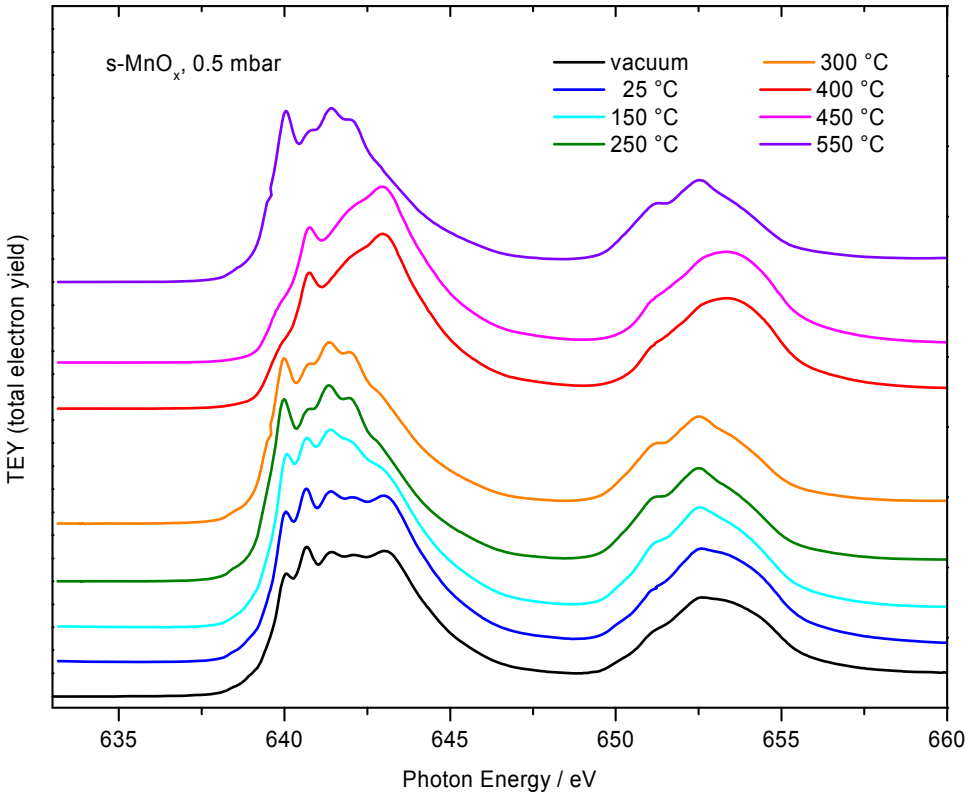

Figure S5. Mn L-NEXAFS spectra of manganese oxide (s-MnO_x) and its decomposition products in 0.5 mbar O_2, at different temperatures.

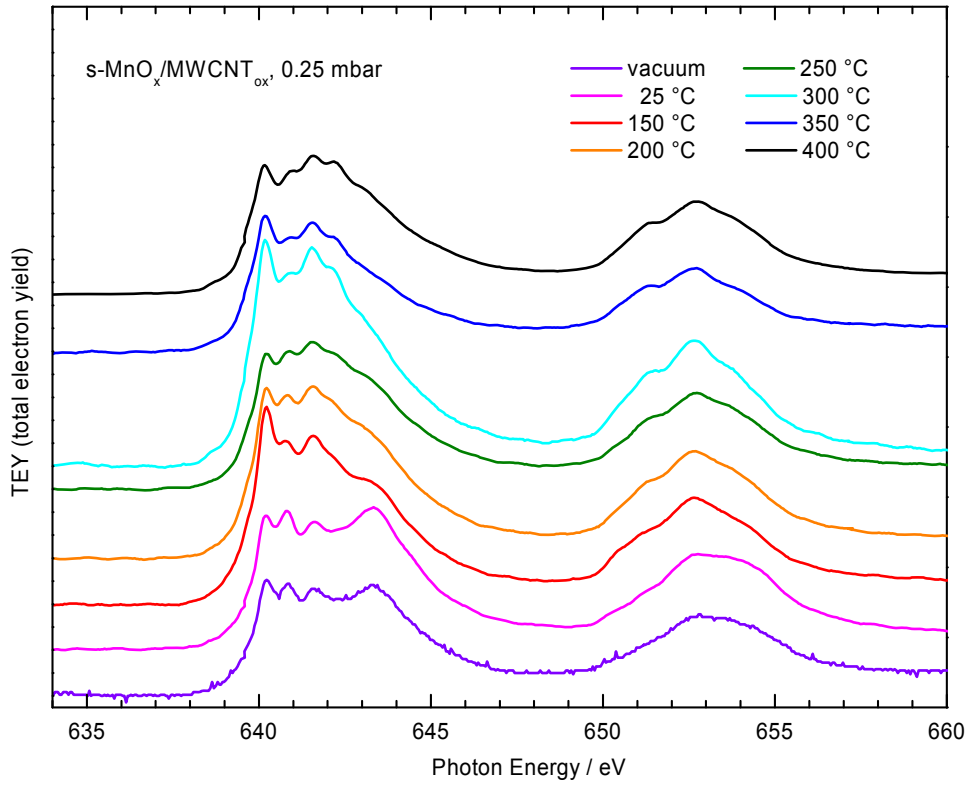

Figure S6. Mn L-NEXAFS spectra of the $MWCNT_{ox}$ supported manganese oxide (s-MnO_x/$MWCNT_{ox}$) and its decomposition products in 0.25 mbar O_2, at different temperatures.

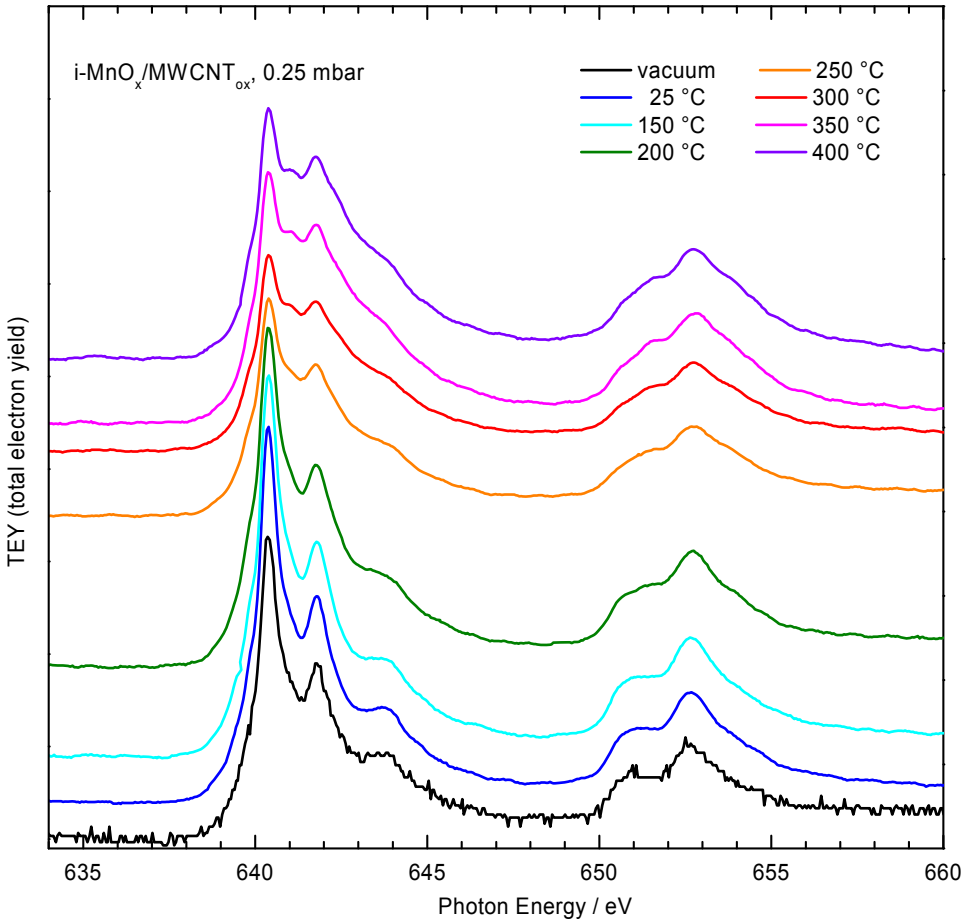

Figure S7. Mn L-NEXAFS spectra of the MWCNT$_{ox}$ supported manganese oxide (i-MnO$_x$/MWCNT$_{ox}$) and its decomposition products in 0.25 mbar O_2, at different temperatures.

Raman

Raman spectroscopy has been used to compare the changes in the nanotubes structure during the two different MnO$_x$ deposition processes. The spectrum of carbon nanomaterials exhibits 3 first-order bands, the G, the D1 and the D2 band. The G (“Graphite”) band at around 1580 cm^{-1} corresponds to an ideal graphitic lattice vibration mode with E_{2g} symmetry. The D bands (“Defect”) are known to be characteristic for disordered graphite and to increase in intensity relative to the G band with increasing degree of disorder in the graphitic structure. The D1 band, which is the most intense of them, appears at ~1360 cm^{-1} and corresponds to a disordered graphitic lattice vibration mode with A_{1g} symmetry. Another band accounting for structural disorder is the D2 band at ~1620 cm^{-1}, which can be observed as a shoulder on the G band. The D2 band corresponds to a disordered graphitic lattice mode with E_{2g} symmetry, like the G band [6].

Raman spectra in Figure S8 show that the s-MnO$_x$/MWCNT$_{ox}$ and i-MnO$_x$/MWCNT$_{ox}$ present a D1 peak centered at 1329 cm^{-1} and 1330 cm^{-1} and another D2 peak with a maximum at 1606 cm^{-1} and 1609 cm^{-1}. The G band is visible at 1583 cm^{-1} and 1584 cm^{-1} respectively. The G and D2 bands are close to the theoretical values for graphite, whereas the D1 band is shifted to lower wavelength. Vidano et al. [7] reported that the position of the D1 band is dependent on the laser wavelength (λ). With increasing λ the D1 band undergoes a shift to lower wavelengths.

To compare the defect density in the nanotubes nanotexture during the two different MnO$_x$ deposition processes the spectra of s-MnO$_x$/MWCNT$_{ox}$ and i-MnO$_x$/MWCNT$_{ox}$ were normalized. The resulting spectra are in reasonable agreement. Hence, no difference in the density of defects can be observed for both MnO$_x$/MWCNT$_{ox}$samples.

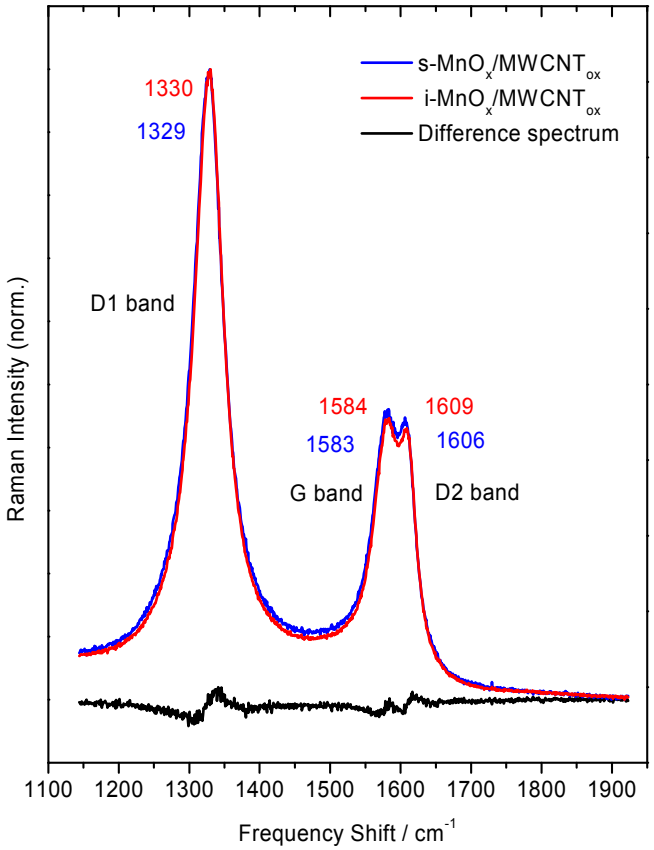

Figure S8. Raman spectra of s-MnO$_x$/MWCNT$_{ox}$ (blue) and i-MnO$_x$/MWCNT$_{ox}$ (red).

XPS

Experimental

The XPS experiments have been obtained using the synchrotron radiation facility BESSY (Berliner Elektronenspeicherringgesellschaft für Synchrotronstrahlung) located in Berlin, Germany. In situ XP spectra have been recorded in 0.5 mbar O_2 (s-MnOx) and 0.25 mbar O_2 (s-MnO$_x$/MWCNT$_{ox}$, i-MnO$_x$/MWCNT$_{ox}$) while heated with a constant rate (6 Kpm) from 25 °C up to 550 °C. XPS data have also been recorded in vacuum and at initial and final state. The beamline has been operated with a 60 µm exit slit. Total Electron Yield (TEY) spectra have been obtained in CMM mode (0.178 eV/s). For the detection of the Mn 2p$_{3/2}$- and Mn 2p$_{1/2}$-orbitals, a energy range of 636 to 663 eV, was measured and for the C 1s-orbitals a range of 282 to 295 eV. About 11 mg of the powder samples were pressed into pellets (dia.: 8 mm) and mounted inside a reaction cell onto a sample holder. Heating is monitored by a thermocouple attached directly to the sample surface. Data have been pre-edge normalized to 1, a constant background has been subtracted and finally, edge jump normalized to 1.

Results and Discussion

Information about the oxidation state of Mn at the surface is obtained with XP spectroscopy. However, the interpretation of the XP spectra with respect to the effective oxidation state of manganese is challenging, because of the broad peak widths and asymmetric peak profiles. The addition of O_2 also reinforces the noise through the interaction of the gas with the electrons. Therefore a low oxygen partial pressure was used. The spectra of s-MnO$_x$, s-MnO$_x$/MWCNT$_{ox}$ and i-MnO$_x$/MWCNT$_{ox}$ are shown in Figure S9, S10 and S11 and Table S1, S2 and S3, respectively. From the relative peak positions and the 2p$_{3/2}$- 2p$_{1/2}$-orbitals no reliable phase mapping of the manganese oxides was possible. In addition, the XPS signal could not be adapted satisfactorily to a single component, which suggests the presence of a mixture, in agreement with the NEXAFS results presented in the main paper. XPS is a more surface sensitive method and it is known that the oxidation states on the surface can vary from the bulk. Therefore, the oxidation states and transition temperatures determined from XPS measurements are not representative for the calcination in air and can only provide general information on the behaviour of the prepared samples. To investigate the near surface oxidation states, more reliable NEXAFS measurements were carried out, which can be interpreted in a more straightforward manner and as presented in the main paper.

In addition, C1s spectra of the MWCNT$_{ox}$-supported samples are compared in Figure S12 to check for significant changes in the carbon phase due to the different synthesis conditions, i.e. the more oxidizing treatment in case of s-MnO$_x$/MWCNT$_{ox}$ due to the presence of MnO_4^- during preparation. Only minor differences are detected indicating that, in agreement with the Raman results, the defect structure of the MWCNT$_{ox}$ material has not been significantly altered.

Substance	Mn $2p_{3/2}$ BE / eV	Mn $2p_{1/2}$ BE / eV	Δ BE / eV
s-MnO_x, vacuum	641.7	653.3	11.6
s-MnO_x, 25 °C, 0.5 mbar O_2	641.5	653.1	11.6
s-MnO_x, 550 °C, 0.5 mbar O_2	641.1	652.7	11.6

Table S1. Data of XP spectra of s-MnO_x under various conditions.

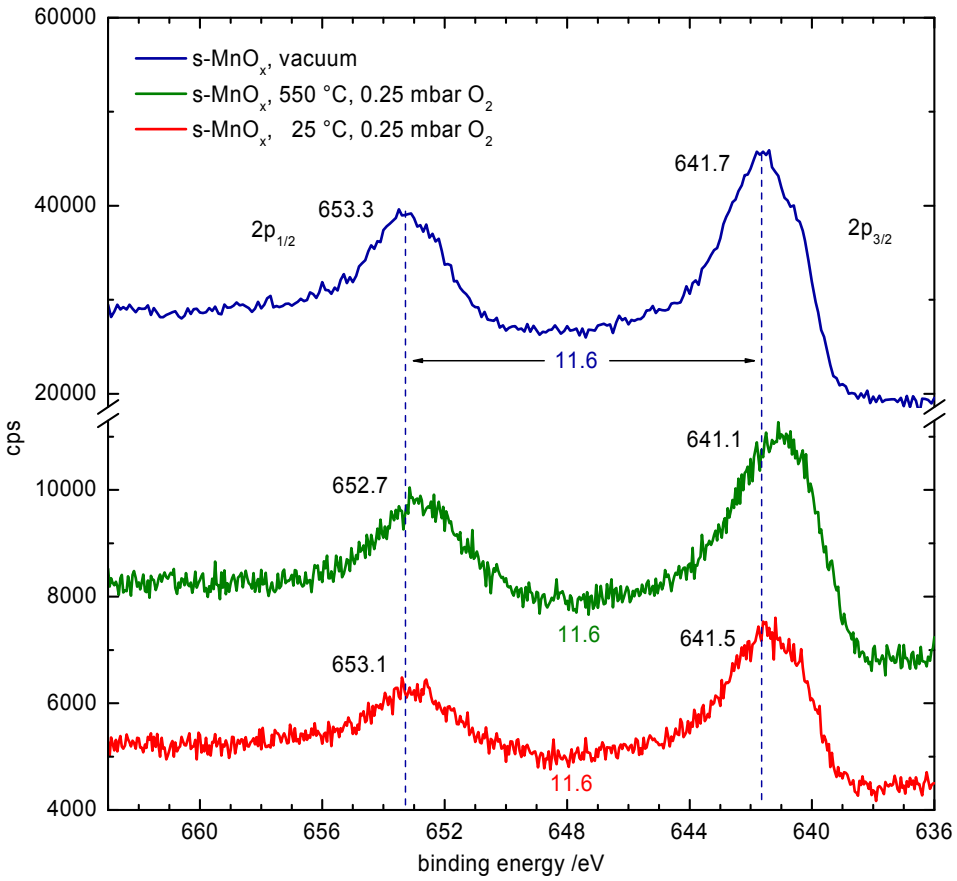

Figure S9. Mn 2p XP spectra of s-MnO_x under various conditions.

Substance	Mn $2p_{3/2}$ BE / eV	Mn $2p_{1/2}$ BE / eV	Δ BE / eV
s-MnO_x/$MWCNT_{ox}$, vacuum	642.0	653.8	11.8
s-MnO_x/$MWCNT_{ox}$, 25 °C, 0.25 mbar O_2	642.0	653.7	11.7
s-MnO_x/$MWCNT_{ox}$, 400 °C, 0.25 mbar O_2	642.6	654.2	11.6

Table S2. XPS data of s-MnO_x/$MWCNT_{ox}$ under various conditions.

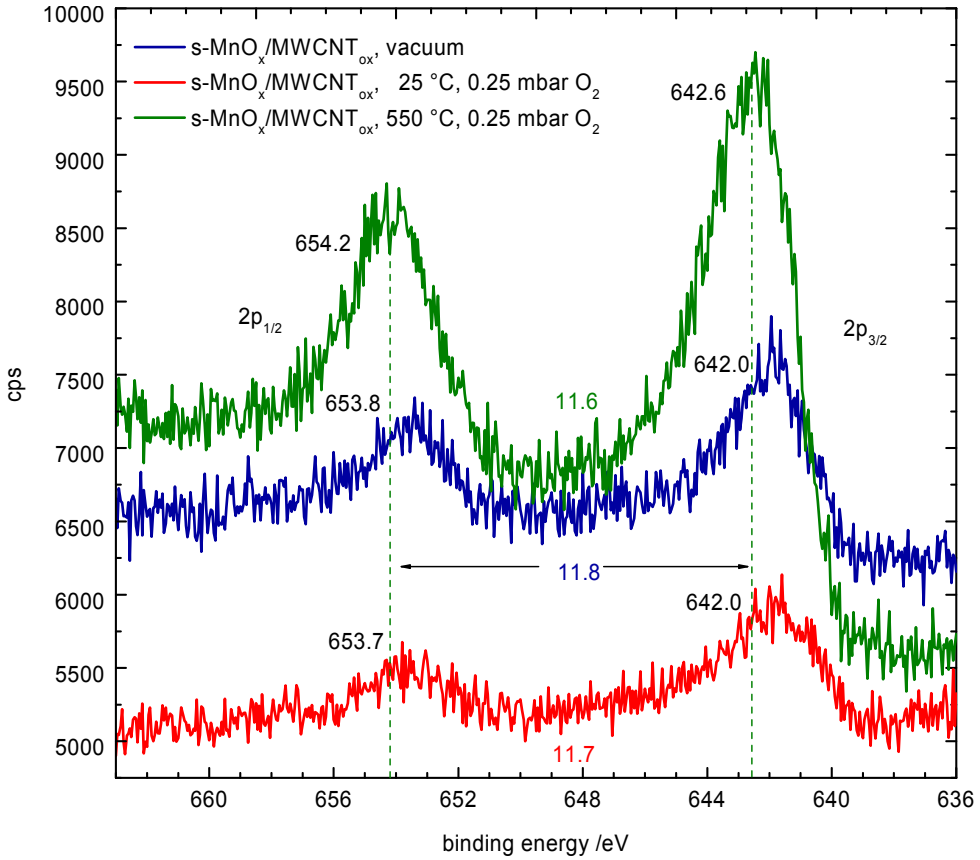

Figure S10. Mn 2p XP spectra of s-MnO$_x$/MWCNT$_{ox}$ under various conditions.

Substance	Mn 2p$_{3/2}$ BE / eV	Mn 2p$_{1/2}$ BE / eV	Δ BE / eV
i-MnO$_x$/MWCNT$_{ox}$, vacuum	642.1	653.7	11.6

Table S3. XPS data of i-MnO$_x$/MWCNT$_{ox}$ in vacuum.

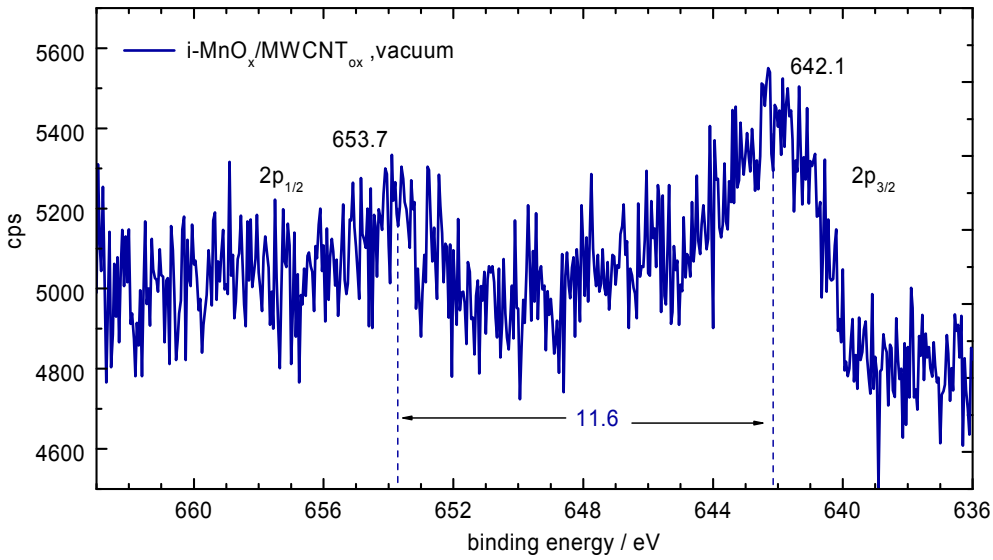

Figure S11. Mn 2p XP spectra of i-MnO$_x$/MWCNT$_{ox}$ in vacuum.

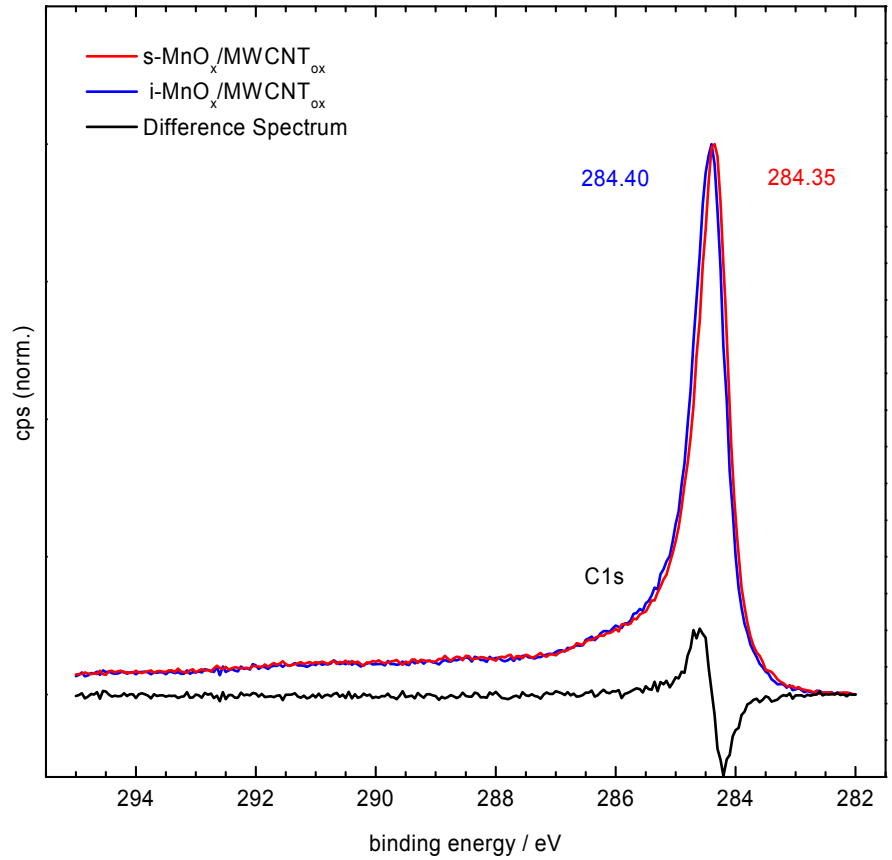

Figure S12. C 1s XP spectra of s-MnO_x/$MWCNT_{ox}$ (red) and i-MnO_x/$MWCNT_{ox}$ (blue) in vacuum.

Literature

[1] A. Peigney, C. Laurent, E. Flahaut, R. R. Bacsa, A. Rousset, *Carbon* **2001**, 39, 507-14.

[2] K. S. W. Sing, D. H. Everett, R. A. W. Haul, L. Moscou, R. A. Pierotti, J. Rouquerol, T. Siemieniewska, *Pure Appl. Chem.* **1985**, 57, 603-619.

[3] A. Peigney, C. Laurent, E. Flahaut, R. R. Bacsa, A. Rousset, *Carbon* **2001** 39, 507-14.

[4] S. P. Cramer, F. M. F. deCroot, Y. Ma, C. T. Chen, F. Sette, C. A. Kipke, D. M. Eichhorn, M. K. Chan, W. H. Armstrong, E. Libby, G. Christou, S. Brooker, V. McKee, O. C. Mullins, J. C. Fuggle, *J. Am. Chem. Soc.* **1991**, 113, 7937-7940.

[5] M. M. Grush, J. Chen, T. L. Stemmler, S. J. George, C. Y. Ralston, R. T. Stibrany, A. Gelasco, G. Christou, S. M. Gorun, J. E. Penner-Hahn, S. P. Cramer, *J. Am. Chem. Soc.* **1996**, 118, 65-69.

[6] A. Sadezky, H. Muckenhuber, H. Grothe, R. Niessner, U. Pöschl, *Carbon* **2005**, 43, 1731-1742.

[7] R. P. Vidano, D. B. Fischbach, L. J. Willis, T. M. Loehr, *Solid State Commun.* **1981**, 39, 341-344.